Available online at www.sciencedirect.com
ScienceDirect
Trans. Nonferrous Met. Soc. China 32(2022) 1598−1608
Transactions of Nonferrous Metals Society of China
www.tnmsc.cn

In-situ hydrothermal synthesis of Ni−MoO_2 heterostructure on porous bulk NiMo alloy for efficient hydrogen evolution reaction

Jian TANG[1], Ji-lin XU[1], Liang-liang LI[1], Yong-cun MA[1], Zhi-guo YE[1], Hong-yu LUO[2], Jun-ming LUO[1]

1. School of Materials Science and Engineering, Nanchang Hangkong University, Nanchang 330063, China;
2. School of Business, Macau University of Science and Technology, Macau 999078, China

Received 17 April 2021; accepted 22 December 2021

Abstract: The Ni−MoO_2 heterostructure was synthesized in suit on porous bulk NiMo alloy by a facile powder metallurgy and hydrothermal method. The results of field emission scanning electron microscopy (SEM), field emission transmission electron microscopy (TEM) and X-ray photoelectron spectroscopy (XPS) reveal that the as-prepared electrode possesses the heterostructure and a layer of $Ni(OH)_2$ nanosheets is formed on the surface of Ni−MoO_2 electrode simultaneously after hydrothermal treatment, which provides abundant interface and much active sites, as well as much active specific surface area. The results of hydrogen evolution reaction indicate that the Ni−MoO_2 heterostructure electrode exhibits excellent catalytic performance, requiring only 41 mV overpotential to reach the current density of 10 mA/cm^2. It also possesses a small Tafel slope of 52.7 mV/dec and long-term stability of electrolysis in alkaline medium.

Key words: hydrogen evolution reaction; Ni−MoO_2 heterostructure; powder metallurgy; porous bulk electrocatalyst; NiMo alloy

1 Introduction

Hydrogen generation from water splitting, driven by intermittent clean energy such as solar energy, wind energy, and tidal energy, is considered as one of the most promising and appealing options for meeting rising energy demands and addressing environmental issues [1−4]. The researchers have paid more attention to alkaline water splitting due to the mild environment. However, the hydrogen evolution reaction (HER) on the cathode still requires to consume extra energy, causing slow HER dynamics, and especially the H—OH bond cleaving in an alkaline medium is much more complicated than in an acidic medium [5−7]. Pt-based electrodes are state-of-the-art HER catalysts, but their low abundance and high cost have limited their industrial applications [8,9]. Thus, designing and developing low-cost and highly efficient non-noble metal HER electrocatalysts has become the goal of researchers.

In the past, the earth-abundant transition metal-based materials with high catalytic activity have been widely explored and made enormous progress in HER, such as phosphides [10,11], disulfides [12,13], and Ni-based alloys [14,15]. Among them, metal−metal oxide is an essential class of materials, such as Ni−NiO [16], Ni−CeO_2 [17], Ni−MoO_2 [18], and Co−Co_3O_4 [19]. Many researchers are interested in the metal−metal oxide heterostructure electrocatalysis materials because they have better HER catalytic performance than their single counterparts due to the synergistic effect of heterostructure at the interface between different components, which can

Corresponding author: Ji-lin XU, Tel: +86-791-83863034, E-mail: jlxu@nchu.edu.cn;
Jun-ming LUO, Tel: +86-791-83953271, E-mail: jmluo@nchu.edu.cn
DOI: 10.1016/S1003-6326(22)65896-5

effectively regulate the surface charge state of the catalysts [20−22]. MoO_2 is a transition metal oxide with a distorted rutile structure and has been studied due to the high potential as non-noble metal HER electrocatalyst for water splitting [23,24]. However, the hydrogen absorption Gibbs free energy change (ΔG_{H^*}) of MoO_2 is positive, which is weak for the absorption of the hydrogen atom. However, the MoO_2 combined with Ni, whose ΔG_{H^*} is negative, can make the ΔG_{H^*} close to that of Pt in theory, which means that it has a more efficient hydrogen evolution ability. Recent studies have shown that the Ni−MoO_2 electrocatalyst displayed excellent HER catalytic performance. For instance, WANG et al [25] reported that the Ni−MoO_2 hetero-structure on the wall of carbon cloth by a three-step approach (electrochemical deposition, hydrothermal treatment and calcination) showed excellent HER catalytic performance in wide pH ranges. ZHOU et al [26] used stereotaxically-constructed graphene as a substrate to synthesize Ni−MoO_2@SCG nano-particle heterojunction, showing excellent HER performance, and even a cell voltage of 1.548 V in water splitting. FAID et al [27] synthesized Ni−MoO_2 nanosheet, and it could achieve cell voltage of 2 V at a current density of 1.15 A/cm^2 in 1 mol/L KOH, and they found that the softening of the water could boost OH^- transport and the anion fumion ionomer led to the decrease of HER activity. DENG et al [28] prepared Ni−MoO_2 nanosheets via the hydrothermal- annealing method. The fabricated electrode required an overpotential of 73 mV to reach a current density of 10 mA/cm^2 for HER in an alkaline medium.

In this work, the porous bulk NiMo alloy was prepared by the microwave sintering, and then the Ni−MoO_2 heterostructure was obtained by the hydrothermal alkalization treatment. This porous bulk NiMo could be directly used as a self-supporting electrocatalyst without a binder. In addition, NiMo alloy showed superior HER performance in an alkaline medium [13,29]. Compared to the nanoparticle electrocatalytic materials, the as-prepared bulk NiMo alloys showed the potential practical application due to their excellent electrocatalytic performance and outstanding stability. The NiMo alloy could transform into Ni−MoO_2 heterostructure after hydrothermal treatment, which could further significantly enhance HER performance close to that of the Pt/C electrode. This method makes the porous bulk material exhibit excellent catalytic performances comparable to or even better than those of some nanostructured catalysts. At the same time, this work also provides some ideas for the preparation of high performance electrocatalysts by powder metallurgy method.

2 Experimental

2.1 Materials

Commercially available metallic Ni (~3 μm, purity >99.9%) and Mo (~3 μm, purity >99.9%) powders were purchased from Beijing Xingrongyuan Technology Co., Ltd., China. All the chemicals used in this work were of analytical grade without further treatment. The chemicals, including ammonium bicarbonate (NH_4HCO_3), sodium hydroxide (NaOH), and potassium hydroxide (KOH), were purchased from Xilong Chemical Co., Ltd., China.

2.2 Synthesis of porous bulk Ni−MoO_2 electrode

The porous NiMo alloy was fabricated by sintering the mixture of Ni and Mo powders at the molar ratio of 6:4, coupled with 10 wt.% NH_4HCO_3 powders (<75 μm) as space holder agent. The Ni−Mo−NH_4HCO_3 mixed powders were blended in a planetary ball mill (QM−3SP4, Nanjing University Instrument Plant, China) at a rotation speed of 200 r/min for 6 h. Then, the blended powders were cold-pressed into green compacts with the dimension of d11 mm × 6 mm through a uniaxial pressure of 775 MPa for 60 s. Subsequently, the green compacts were placed into an insulation barrel. Finally, the insulation barrel was put into a 2.45 GHz, 5 kW continuously adjustable micro-wave sintering furnace (NJZ4−3, Nanjing Juequan Co., Ltd., China). The green compacts were heated up to 900 °C with a heating rate of 20−30 °C/min for 20 min and then cooled with the furnace. During the sintering process, the microwave furnace was filled with flowing high-purity argon gas (purity >99.999%) to prevent the oxidation of the sintered samples. For the specific preparation process, it could be referred in our previous work [30,31].

The porous bulk Ni−MoO_2 electrode was synthesized by hydrothermal treatment. In a typical process, the sintered porous NiMo alloy was firstly

dislodged from surface oxide layer and cleaned in de-ionized (DI) water for 10 min under continuous ultrasound. Then, the cleaned sample and 15 mL 5.0 mol/L sodium hydroxide aqueous solution were transferred to a 20 mL Teflon-lined stainless-steel autoclave, and held at 150 °C for 28 h in a drying oven. After cooling down, the sample was taken out and washed with DI water and ethanol several times. Finally, the sample was dried at 60 °C for 10 h.

2.3 Characterization

The phase composition of the samples was characterized by X-ray diffraction (XRD, Bruker D8 ADVANCE, Germany) with Cu K_α as radiation source (λ=0.154 nm) at a scanning rate of 2 (°)/min. The field emission scanning electron microscope (FESEM, FEI Nova Nano SEM450, USA) was employed to investigate the surface morphologies of the samples at an acceleration voltage of 15 kV. The field emission transmission electron microscope (TEM, FEI Talos F200x, USA) was employed at an acceleration voltage of 200 kV, and a focused ion beam (FIB, FEI Helios Nanolab 600i, USA) was employed to prepare the TEM sample. The chemical composition and electronic states of the samples were examined using an X-ray photoelectron spectroscopy (XPS, Shimadzu Kratos Axis Ultra DLD, Japan) with a standard monochromatic Al K_α source (150 W, 10 mA, 15 kV).

2.4 Electrochemical measurement

The electrochemical workstation (CHI650D, Shanghai Chenhua Instrument Co., Ltd., China) with a standard three-electrode system was used to carry out the electrochemical tests of the prepared HER electrodes in 1.0 mol/L KOH solution. The Ni−MoO_2 electrode with the exposed area of 1 cm^2, the saturated calomel electrode (SCE), and the graphite electrode were served as the working electrode, reference electrode and counter electrode, respectively. The polarization curves were carried out using linear sweep voltammetry (LSV) at a scan rate of 1 mV/s. The electrochemical impedance spectroscopy (EIS) was measured at open circuit potential in the frequency ranging from 100 kHz to 0.01 Hz. To obtain the double layer capacitance (C_{dl}), cyclic voltammetry (CV) from 0.3 to 0.4 V (vs RHE) was tested with different scan rates (from 10 to 100 mV/s). The electrochemical stabilities were measured by chronopotentiometry (CP) at different constant current densities of 10, 100 and 200 mA/cm^2, and 3000 cycles continuous cyclic voltammetry with a sweep rate of 100 mV/s from 0 to −0.5 V (vs RHE) was used to evaluate the stability of the sample.

3 Results and discussion

3.1 Microstructure of Ni−MoO_2 electrode

To confirm the crystal structure and phase composition of Ni−MoO_2 sample, the XRD patterns of Ni−MoO_2 catalyst are shown in Fig. 1. The Ni−MoO_2 catalyst is mainly composed of MoO_2 phase except for the metallic Mo and Ni phases from the NiMo alloy substrate. The diffraction peaks located at 2θ=40.5°, 58.6°, and 73.7° correspond to (110), (200) and (211) crystal planes of metallic Mo (JCPDS No. 42-1120). At the same time, the peaks located at 2θ=26.08°, 37.02°, and 53.5°, being attributed to MoO_2 (JCPDS No. 32-0637), are also detected. In addition, the peaks located at 2θ=43.5°, 50.8°, and 74.5°, should be assigned to metallic Ni (JCPDS No. 04-0850). Due to the similar atom diameter of Ni and Mo, a small amount of Mo atom is dissolved into the Ni lattice, resulting in the lattice distortion of Ni and the corresponding diffraction peaks moving to smaller angles [32]. In order to reveal the characteristics of surface morphologies of the as-prepared catalysts, the FESEM images of porous NiMo and Ni−MoO_2 samples are displayed in Fig. 2. Many large pores are randomly distributed over the surface of the NiMo alloy (Fig. 2(a)), and a large number of 3D-interconnected small stone-like particles are

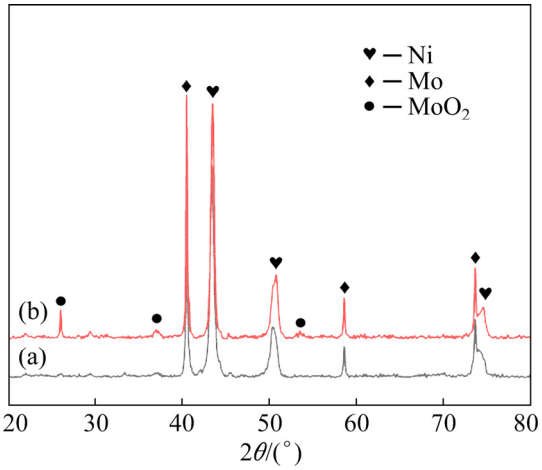

Fig. 1 XRD patterns of porous NiMo alloy (a) and Ni−MoO_2 (b)

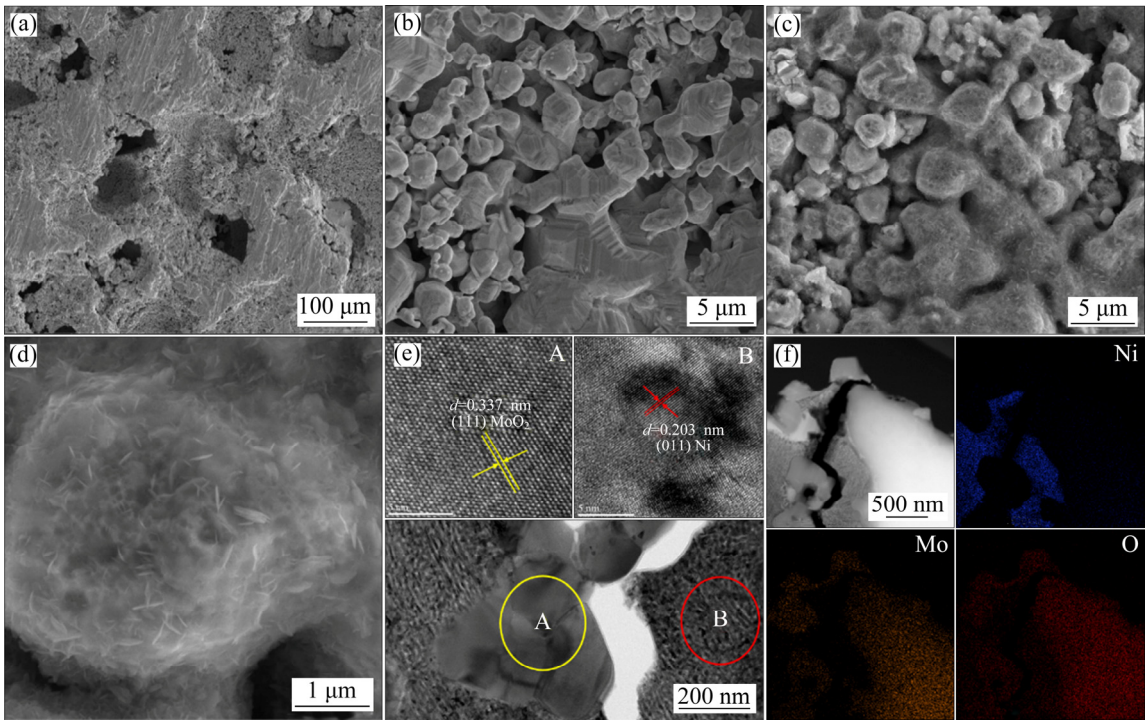

Fig. 2 SEM images of porous NiMo alloy (a, b) and Ni−MoO_2 (c, d); TEM image and corresponding high-resolution TEM image (e); high-angle annular dark-field (HAADF)-STEM image and elemental mappings of Ni−MoO_2 (f)

distributed inside the large pores (Fig. 2(b)). This intricate porous structure is mainly attributed to the pore-forming effect of NH_4HCO_3 and the Kirkendall effect between Ni and Mo atoms [30]. This intricate porous structure makes the bulk catalyst obtain a huge specific surface area to expose more active sites for HER. After hydrothermal treatment, the stone-like particles become fluffy, and a layer of three-dimensional needle and flake-like structure on the surface can be observed (Figs. 2(c, d)), which may further enhance the HER performance. To further prove the phase and structure of Ni−MoO_2 catalyst, HRTEM image is shown in Fig. 2(e). The TEM image can be divided into two regions. The lattice fringe for Region A with an interplanar spacing of 0.337 nm corresponds to $(\bar{1}11)$ crystal plane of MoO_2. The lattice fringe for Region B with an interplanar spacing of 0.203 nm is assigned to (011) crystal plane of metallic Ni. Additionally, the high-angle annular dark-field scanning-TEM (HAADF-STEM) image in Fig. 2(f) shows the existence of Ni, Mo and O elements, and displays the area of Ni and Mo elements, which indicates that the porous NiMo alloy has produced the heterostructure after hydrothermal treatment.

3.2 XPS analysis results of Ni−MoO_2 electrode

The X-ray photoelectron spectroscopy (XPS) was carried out to further investigate the surface chemical composition and valence states of Ni−MoO_2 catalyst. As shown in Fig. 3(a), the survey spectrum shows the existence of C, O, Ni, and Mo in as-prepared Ni−MoO_2 catalyst, and the binding energy of the constituent elements is calibrated by carbon contamination at 284.8 eV before peaks are fitted (Fig. 3(b)) [33]. As presented in the high-resolution XPS spectrum of Ni 2p (Fig. 3(c)), the peaks located at binding energy of 856.1 and 873.7 eV with strong shakeup satellites at 862.3 and 880.3 eV can be ascribed to Ni $2p_{3/2}$ and Ni $2p_{1/2}$ of Ni^{2+} species, respectively [34]. From the Mo 3d spectrum in Fig. 3(d), the deconvoluted peaks at 230.8 and 233.9 eV can be assigned to the Mo $3d_{5/2}$ and Mo $3d_{3/2}$ of Mo^{4+}, while peaks located at 232.5 and 235.6 eV can be attributed to Mo^{6+}, which mainly results from the sample surface oxidation in the air environmental [35−37]. Furthermore, in the high-resolution XPS spectra of O 1s (Fig. 3(e)), the characteristic peaks located at 530.8, 531.5 and 532.8 eV present the existence of Mo—O band, surface —OH group and adsorbed oxygen on the surface, respectively [38,39]. The

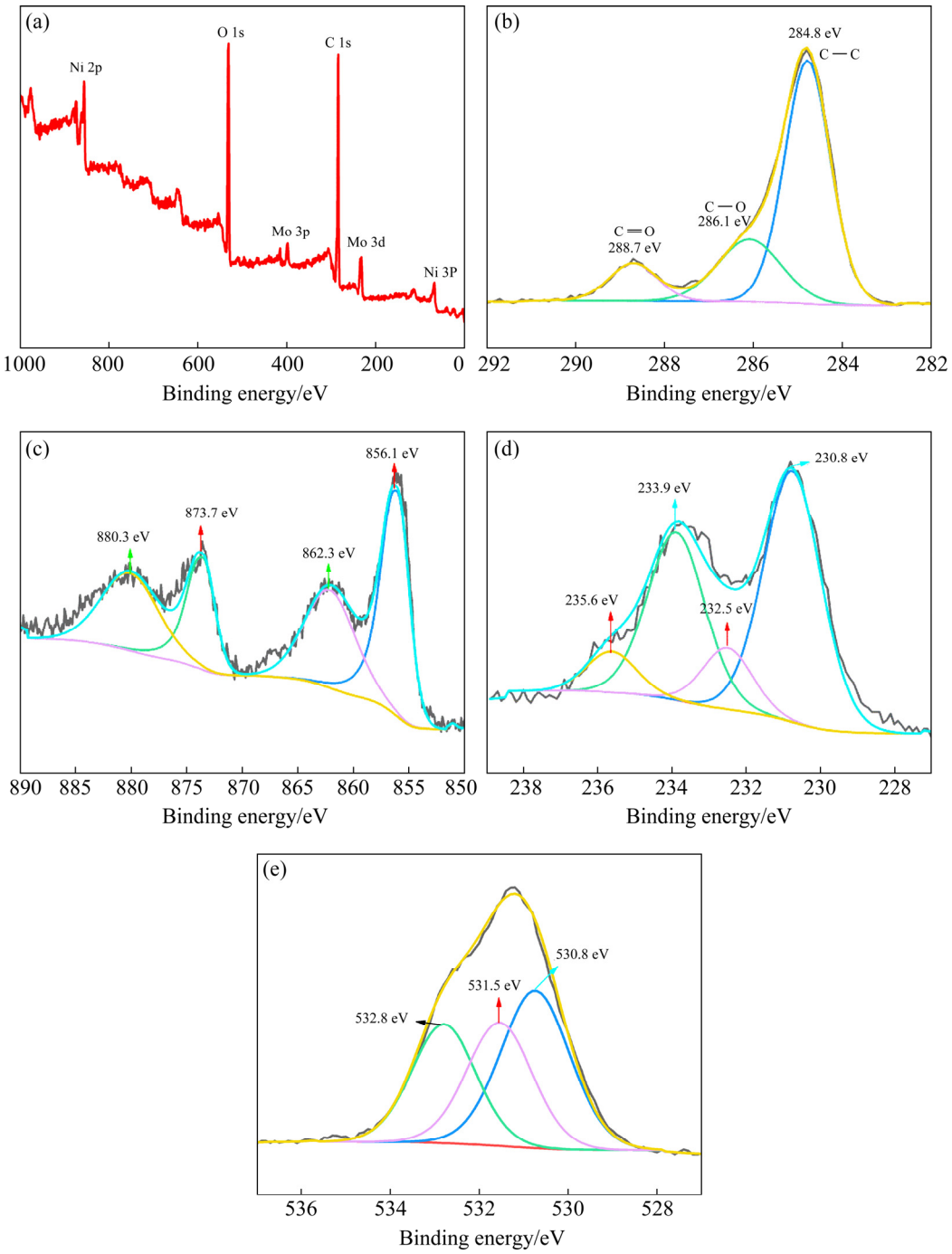

Fig. 3 XPS spectra of Ni−MoO_2 catalyst: (a) Survey; (b) C 1s; (c) Ni 2p; (d) Mo 3d; (e) O 1s

results indicate that Mo on the electrode surface mainly exists in the form of MoO_2, and the metallic Ni on the surface of the sample will be transformed into $Ni(OH)_2$ with high catalytic activity in an alkaline hydrothermal environment.

3.3 HER performance of Ni−MoO_2 electrode

The electrocatalytic HER activities of the as-prepared NiMo, Ni−MoO_2 and Pt/C electrocatalysts were evaluated in 1.0 mol/L KOH solution with a typical three-electrode system. The polarization curves with IR-correction were obtained at a scan rate of 1 mV/s. For comparison, the commercial Pt/C powder was loaded on the glassy carbon electrode with a mass loading of 0.42 mg/cm^2 and the polarization curve was measured under the same experimental condition. As shown in Fig. 4(a), the Ni−MoO_2 heterostructure exhibits superior HER

performance with an overpotential of 41 mV to reach the current density of 10 mA/cm^2, which is close to that of Pt/C (33 mV). Fortunately, the overpotentials for Ni−MoO_2, NiMo, Pt/C electrocatalyst are 109.8, 213.2 and 97 mV, respectively, when the current density approaches 100 mA/cm^2. In addition, compared to some other metal−metal oxide catalysts (listed in Table 1), the as-prepared Ni−MoO_2 heterostructure has quite strong competitiveness and expresses the high potential for water splitting [22,25−28,40−44].

Besides overpotential, the Tafel slope obtained from the LSV curves is also an important parameter to evaluate the HER reaction kinetics [45,46]. According to the literatures [47−49], the main reaction of HER can be divided into two steps in alkaline solution, namely the dissociation of H_2O to form the intermediate state of H* (Volmer step) and the adsorption of H* to form H_2 (Tafel step or Heyrovsky step). At the same time, the three different Tafel slopes, including 118, 39 and 29 mV/dec, correspond to the rate-determining step (RDS) of Volmer (RDS)−Heyrovsky (or Tafel), Volmer−Heyrovsky (RDS) and Volmer−Tafel (RDS), respectively [50,51]. As displayed in Fig. 4(b), the Tafel slopes are 125.2, 52.7 and 42.4 mV/dec for porous NiMo alloy, Ni−MoO_2, and Pt/C, respectively, indicating that the as-prepared catalysts follow the Volmer−Heyrovsky mechanism and the RDS of Ni−MoO_2 changes from the water dissociation reaction to the adsorption of H*.

Electrochemical impedance spectra (EIS) were further used to analyze the HER kinetics and measured at open circuit potential. The Nyquist plots with a fitted equivalent circuit are shown in Fig. 5(a), and the fitted parameters are listed in

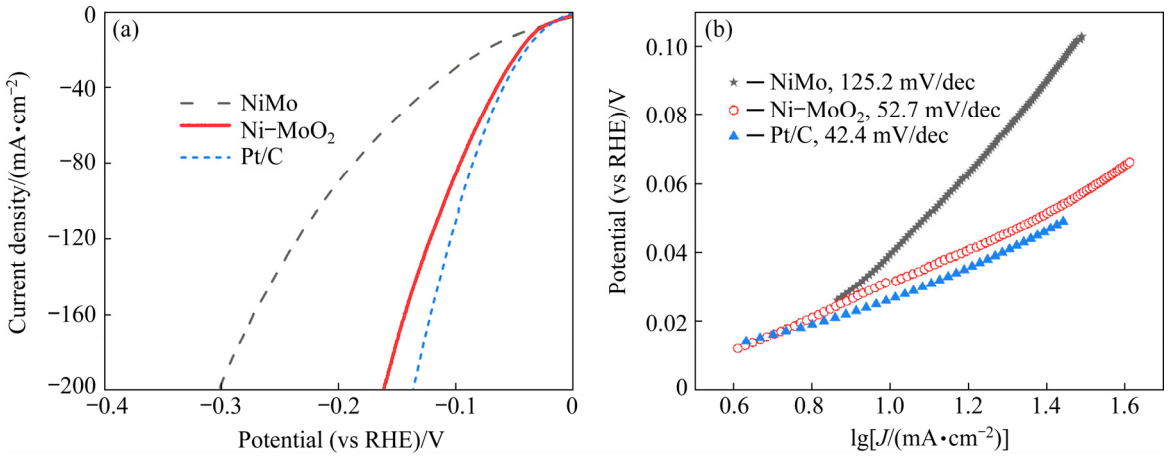

Fig. 4 Polarization curves (a) and corresponding Tafel plots (b) of porous NiMo alloy, Ni−MoO_2, and 20 wt.% Pt/C electrodes in 1.0 mol/L KOH solution

Table 1 Comparison of HER catalytic activity of different catalysts

Catalyst	J/(mA·cm^{-2})	Overpotential/mV	Tafel slope/(mV·dec^{-1})	Ref.
MoO_2−Ni NWs	10	58.4	36.6	[22]
Ni−MoO_2	10	46	56.9	[25]
Ni−MoO_2	10	93	120	[26]
Ni−MoO_2@SCG	10	79.97	53.3	[27]
Ni/MoO_2	10	40	116	[28]
Co/Ni−MoO_2	10	103	80	[40]
Ni/NiO	10	98	79	[41]
NiO/Ni@NCNTs	10	87.5	80	[42]
Ru/Co_3O_4 NWs	10	30.98	69.75	[43]
Fe−NiO/NF	10	183	105.5	[44]
Ni−MoO_2	10	41	52.7	This work

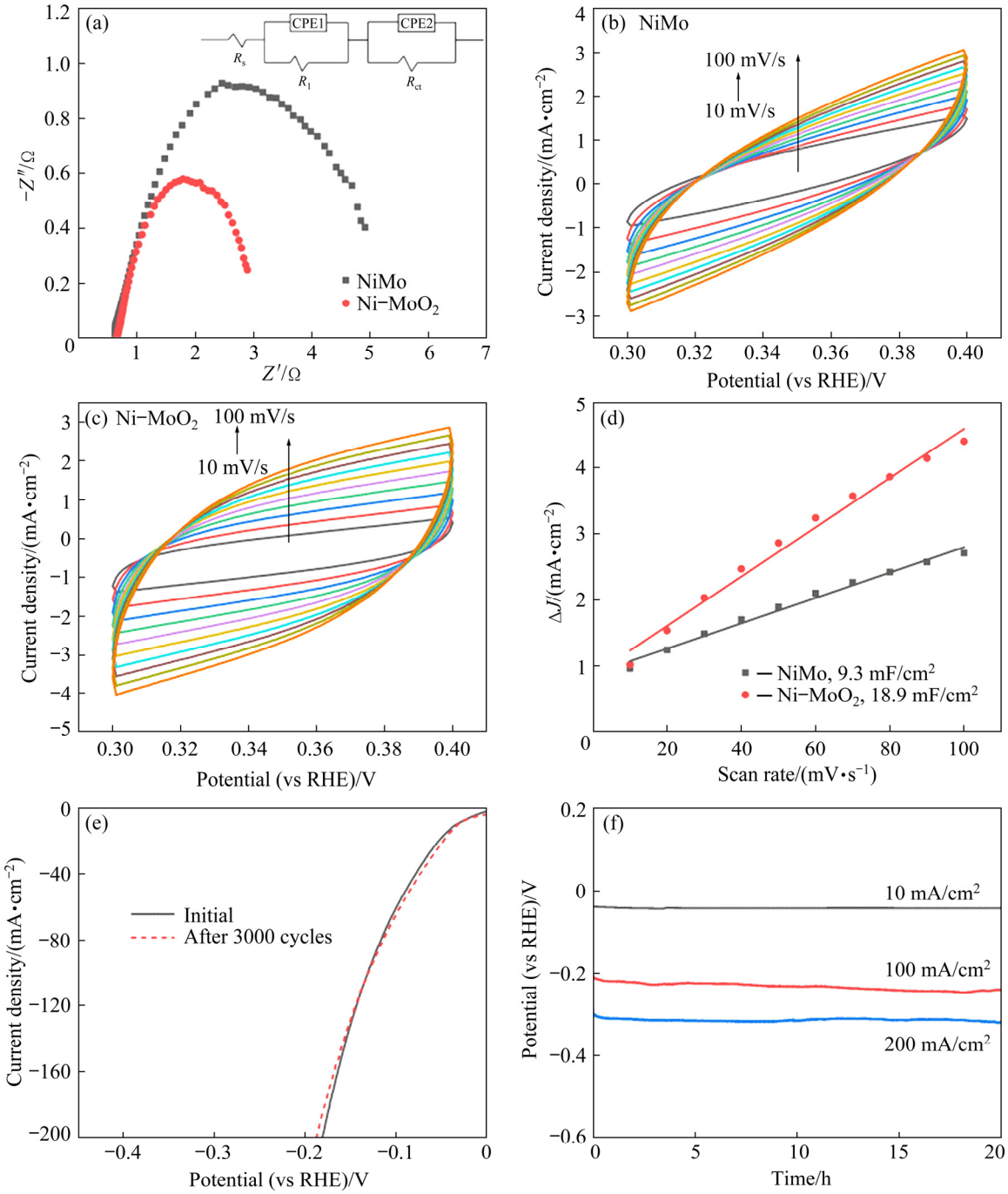

Fig. 5 Nyquist plots (a), cycle voltammograms from 0.3 to 0.4 V (vs RHE) in 1.0 mol/L KOH at different scan rates (b, c), C_{dl} values of NiMo alloy and Ni−MoO_2 (d), LSV curves of Ni−MoO_2 before and after 3000 CV cycles (e), and chronopotentiometry test results of Ni−MoO_2 electrode at constant current density of 10, 100, and 200 mA/cm^2 (without IR-correction) (f)

Table 2. R_1 is assigned to the pores of the surface, and R_s is the electrolyte resistance, which is used to modify the LSV curves [52]. The electron-transfer resistance (R_{ct}) of Ni−MoO_2 is 2.3 Ω, lower than that of the NiMo alloy (4.6 Ω). The result confirms that the Ni−MoO_2 heterostructure can reduce the charge transfer resistance and accelerate the reaction kinetics. Moreover, the electrochemically active surface area (ECSA) was estimated by cyclic voltammetry (CV) at the non-faraday region to obtain double-layer capacitance (C_{dl}). As shown in Figs. 5(b−d), the Ni−MoO_2 displays the C_{dl} value of 18.9 mF/cm^2, much larger than that of the NiMo alloy (9.3 mF/cm^2). This suggests that the NiMo

Table 2 Values of equivalent circuit fitting for Nyquist plots of as-prepared catalysts

Sample	R_s/Ω	R_1/Ω	R_{ct}/Ω
NiMo	0.59	0.5375	4.627
Ni−MoO_2	0.6582	0.2205	2.329

alloy has transformed into Ni−MoO_2 hetero-structure after hydrothermal alkalization treatment and can expose more active sites, directly proven by the SEM images (seen in Figs. 2(c, d)).

In addition to HER activity, the stability of catalysts is an important factor in the practical application of water splitting. The long-term durability tests of Ni−MoO_2 were conducted by cyclic voltammetry (CV) scanning for 3000 cycles with a potential range from 0 to −0.5 V (vs RHE) at a scan rate of 50 mV/s. After sweeping for 3000 cycles, the LSV curve of Ni−MoO_2 is almost consistent with the initial line (Fig. 5(e)). Furthermore, the chronopotentiometry test was carried out to further evaluate the stability of Ni−MoO_2 at a constant current density of 10, 100, and 200 mA/cm^2 for 20 h (Fig. 5(f)), and the almost unchanged potentials indicate the outstanding stability of the as-prepared electrode. At the same time, the phase composition and surface morphology were further investigated. It can be seen from Fig. 6(a) that the diffraction peaks of Ni−MoO_2 electrode do not change significantly after the stability test. Moreover, the lobular nanosheets can be directly observed on the surface by SEM (Fig. 6(b)), which is different from that before HER. Furthermore, the surface electronic valence state was further analyzed after an electrochemical test by XPS. For the Ni 2p narrow scan spectrum (Fig. 6(c)), the fitted peaks are centered at 855.6 eV for Ni $2p_{3/2}$ and 873.7 eV for Ni $2p_{1/2}$, which are assigned to the $Ni(OH)_2$ [53]. In Mo 3d spectrum (Fig. 6(d)), the two distinct peaks located at 232.3 eV and 235.5 eV can be matched to Mo $3d_{5/2}$ and Mo $3d_{3/2}$, respectively, which belong to the Mo—O band of MoO_3 [54]. XPS results indicate that the component of surface nanosheets is assigned to $Ni(OH)_2$ and MoO_3. These results demonstrate that the metal hydroxides are formed, and the structure and composition of Ni−MoO_2 electrode suffer restructure during the HER process.

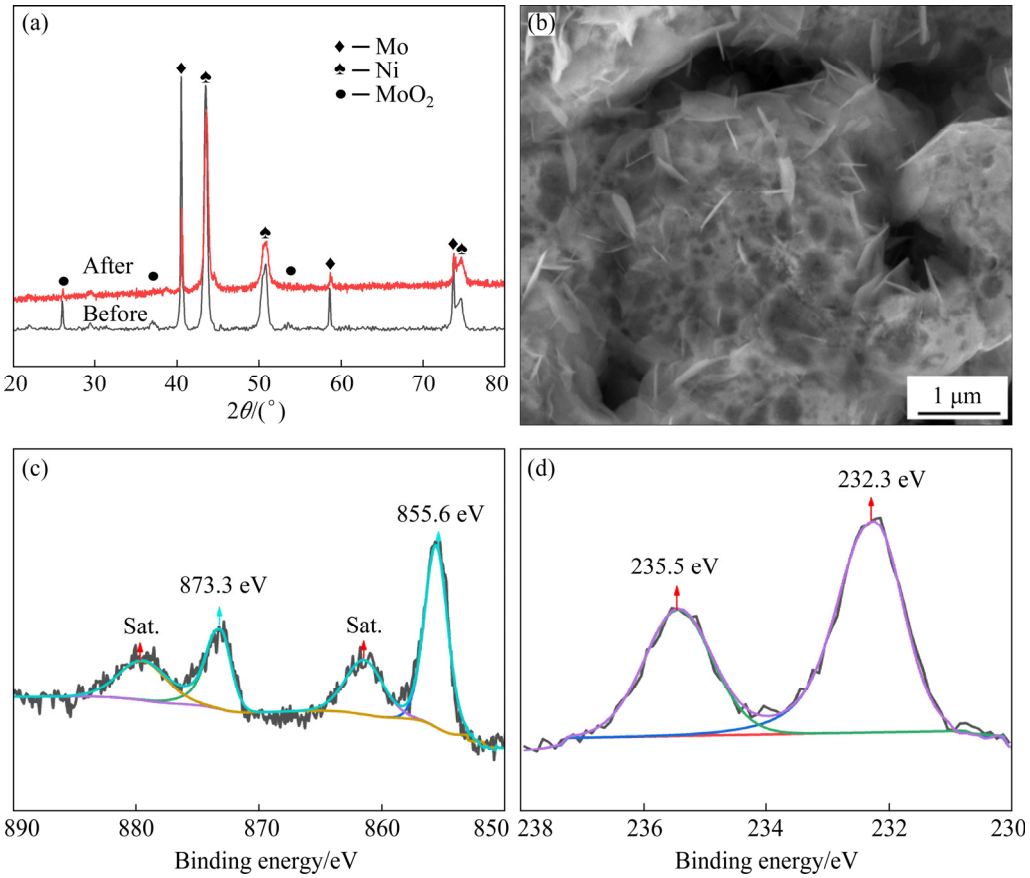

Fig. 6 XRD patterns of Ni−MoO_2 electrode before and after stability test (a); SEM image of Ni−MoO_2 electrode after stability test (b); XPS spectra for Ni 2p (c) and Mo 3d (d) of Ni−MoO_2 electrode after stability test

4 Conclusions

(1) The Ni−MoO_2 heterostructure electrocatalyst is successfully synthesized by microwave sintering and hydrothermal treatment.

(2) The Ni−MoO_2 electrode exhibits the superior HER catalytic performance with a low overpotential of 41 mV to reach the current density of 10 mA/cm^2, and a small Tafel slope of 52.7 mV/dec in 1.0 mol/L KOH solution, which is much better than that of porous NiMo alloy precursor.

(3) The Ni−MoO_2 presents the superior HER performance, attributed to the function of the heterostructure interface, which can enhance the electronic interaction between species, reduce charge transfer resistance and increase the water adsorption on the catalyst.

Acknowledgments

The authors are grateful for the financial supports from the National Natural Science Foundation of China (Nos. 52161040, 51862026), the Natural Science Foundation of Jiangxi Province, China (Nos. 20202ACBL214011, 20192ACBL-21048), and the Aeronautical Science Foundation of China (No. 2017ZF56027).

References

[1] CHU S, MAJUMDAR A. Opportunities and challenges for a sustainable energy future [J]. Nature, 2012, 488: 294−303.

[2] WIJTEN J H J, RIEMERSMA R L, GAUTHEIR J, MANDEMAKER L D B, VERHOEVEN M W G M, HOFMANN J P, CHAN K, WECKHUYSEN B M. Electrolyte effects on the stability of Ni−Mo cathodes for the hydrogen evolution reaction [J]. ChemSusChem, 2019, 12(15): 3491−3500.

[3] MCKONE J R, MARINESCU S C, BRUNSCHWIG B S, WINKLER J R, GRAY H B. Earth-abundant hydrogen evolution electrocatalysts [J]. Chemical Science, 2014, 5: 865−878.

[4] YAO Mao-hai, TANG You-gen, ZHANG Li, YANG Hai-hua, YAN Jian-hui. Photocatalytic activity of CuO towards HER in catalyst from oxalic acid solution under simulated sunlight irradiation [J]. Transactions of Nonferrous Metals Society of China, 2010, 20: 1944−1949.

[5] KOU T, CHEN M, WU F, SMART T J, WANG S, WU Y, ZHANG Y, LI S, LALL S, ZHANG Z, LIU Y S, GUO J, WANG G, PING Y, LI Y. Carbon doping switching on the hydrogen adsorption activity of NiO for hydrogen evolution reaction [J]. Nature Communications, 2020, 11: 590.

[6] LI Zhe, FENG Yi, LIANG Yu-lin, CHENG Chuan-qi, DONG Cun-ku, LIU Hui, DU Xi-wen. Stable rhodium(IV) oxide for alkaline hydrogen evolution reaction [J]. Advanced Materials, 2020, 32: 1908521.

[7] WU Q, LUO M, HAN J, PENG W, ZHAO Y, CHEN D, PENG M, LIU J, de GROOT F M F, TAN Y. Identifying electrocatalytic sites of nanoporous copper-ruthenium alloy for hydrogen evolution reaction in alkaline electrolyte [J]. ACS Energy Letters, 2020, 5(1): 192−199.

[8] MCCRORY C C L, JUNG S, FERRER I M, CHATMAN S M, PETERS J C, JARAMILLO T F. Benchmarking hydrogen evolving reaction and oxygen evolving reaction electrocatalysts for solar water splitting devices [J]. Journal of the American Chemical Society, 2015, 137(13): 4347−4357.

[9] ZHU J, WANG Z C, DAI H, WANG Q, YANG R, YU H, LIAO M, ZHANG J, CHEN W, WEI Z, LI N, DU L, SHI D, WANG W, ZHANG L, JIANG Y, ZHANG G. Boundary activated hydrogen evolution reaction on monolayer MoS_2 [J]. Nature Communications, 2019, 10(1): 1348.

[10] XU K, CHENG H, LV H F, WANG J Y, LIU L Q, LIU S, WU X J, CHU W S, WU C Z, XIE Y. Controllable surface reorganization engineering on cobalt phosphide nanowire arrays for efficient alkaline hydrogen evolution reaction [J]. Advanced Materials, 2018, 30(1): 1703322.

[11] CHEN Y Q, ZHANG J F, WAN L, HU W B, LIU L, ZHONG C, DENG Y D. Effect of nickel phosphide nanoparticles crystallization on hydrogen evolution reaction catalytic performance [J]. Transactions of Nonferrous Metals Society of China, 2017, 27: 369−376.

[12] WANG S, ZHANG D, LI B, ZHANG C, DU Z G, YIN H M, BI X F, YANG S B. Ultrastable in-plane 1T−2H MoS_2 heterostructures for enhanced hydrogen evolution reaction [J]. Advanced Energy Materials, 2018, 8(25): 1801345.

[13] WANG D Y, GONG M, CHOU H L, PAN C J, CHEN H A, WU Y P, LIN M C, GUAN M Y, YANG J, CHEN C W, WANG Y L, HWANG B J, CHEN C C, DAI H J. Highly active and stable hybrid catalyst of cobalt-doped FeS_2 nanosheets–carbon nanotubes for hydrogen evolution reaction [J]. Journal of the American Chemical Society, 2015, 137(4): 1587−1592.

[14] NAIRAN A, ZOU P C, LIANG C W, LIU J X, WU D, LIU P, YANG C. NiMo solid solution nanowire array electrodes for highly efficient hydrogen evolution reaction [J]. Advanced Functional Materials, 2019, 29(44): 1903747.

[15] CHE Q J, BAI N N, LI Q, CHEN X H, TAN Y, XU X. One-step electrodeposition of a hierarchically structured S-doped NiCo film as a highly-efficient electrocatalyst for the hydrogen evolution reaction [J]. Nanoscale, 2018, 10: 15238−15248.

[16] YAN X D, TIAN L H, CHEN X B. Crystalline/amorphous Ni/NiO core/shell nanosheets as highly active electrocatalysts for hydrogen evolution reaction [J]. Journal of Power Sources, 2015, 300: 336−343.

[17] WENG Zhe, LIU Wen, YIN Li-chang, FANG Ruo-pian, LI Min, ALTMAN E I, FAN Qi, LI Feng, CHENG Hui-ming, WANG Hai-liang. Metal/oxide interface nanostructures generated by surface segregation for electrocatalysis [J]. Nano Letters, 2015, 15(11): 7704−7710.

[18] REN B W, LI D Q, JIN Q Y, CUI H, WANG C X. Integrated 3D self-supported Ni decorated MoO_2 nanowires as highly efficient electrocatalysts for ultra-highly stable and large-current-density hydrogen evolution [J]. Journal of Materials Chemistry A, 2017, 5: 24453−24461.

[19] YAN X D, TIAN L H, HE M, CHEN X B. Three-dimensional crystalline/amorphous Co/Co_3O_4 core/shell nanosheets as efficient electrocatalysts for the hydrogen evolution reaction [J]. Nano Letters, 2015, 15(9): 6015−6021.

[20] SONG B, LIN S. Two are better than one: Heterostructures improve hydrogen evolution catalysis [J]. Joule, 2017, 1(2): 220−221.

[21] ZHAO G Q, RUI K, DOU S X, SUN W P. Heterostructures for electrochemical hydrogen evolution reaction: A Review [J]. Advanced Functional Materials, 2018, 28(43): 1803291.

[22] LIU X, NI K, NIU C J, GUO R T, XI W, WANG Z Y, MENG J S, LI J T, ZHU Y W, WU P J, LI Q, LUO J, WU X J, MAI L Q. Upraising the O 2p orbital by integrating Ni with MoO_2 for accelerating hydrogen evolution kinetics [J]. ACS Catalysis, 2019, 9(3): 2275−2285.

[23] JIN Y S, WANG H T, LI J J, YUE X, HAN Y J, SHEN P K, CUI Y. Porous MoO_2 nanosheets as non-noble bifunctional electrocatalysts for overall water splitting [J]. Advanced Materials, 2016, 28(19): 3785−3790.

[24] ZENG H B, CHEN S Q, JIN Y Q, LI J W, SONG J D, LE Z C, LIANG G F, ZHANG H, XIE F Y, CHEN J, JIN Y S, CHEN X B, MENG H. Electron density modulation of metallic MoO_2 by Ni doping for excellent hydrogen evolution and oxidation activities in acid [J]. ACS Energy Letters, 2020, 5(6): 1908−1915.

[25] WANG B Z, HUANG H X, HUANG M L, YAN P X, ISIMJAN T T, YANG X L. Electron-transfer enhanced MoO_2−Ni heterostructures as a highly efficient pH-universal catalyst for hydrogen evolution [J]. Science China Chemistry, 2020, 63: 841−849.

[26] ZHOU T, HUANG Y Q, ALI A, SHEN P K. Ni−MoO_2 nanoparticles heterojunction loaded on stereotaxically-constructed graphene for high-efficiency overall water splitting [J]. Journal of Electroanalytical Chemistry, 2021, 897: 115555.

[27] FAID A Y, BARNETT A O, SELAND F, SUNDE S. Tuning Ni−MoO_2 catalyst−ionomer and electrolyte interaction for water electrolyzers with anion exchange membranes [J]. ACS Applied Energy Materials, 2021, 4(4): 3327−3340.

[28] DENG S F, LIU X P, HUANG T, ZHAO T H, LU Y, CHENG J Y, SHEN T, LIANG J N, WANG D L. MoO_2 modulated electrocatalytic properties of Ni: Investigate from hydrogen oxidation reaction to hydrogen evolution reaction [J]. Electrochimica Acta, 2019, 324: 134892.

[29] GIAO W, GOU W Y, ZHOU X M, HO J C, MA Y Y, QU Y Q. Amine-modulated/engineered interfaces of NiMo electrocatalysts for improved hydrogen evolution reaction in alkaline solutions [J]. ACS Applied Materials and Interfaces, 2018, 10(2): 1728−1733.

[30] XU J L, ZHANG J L, BAO L Z, LAI T, LUO J M, ZHENG Y F. Preparation and bioactive surface modification of the microwave sintered porous Ti−15Mo alloys for biomedical application [J]. Science China Materials, 2018, 61(4): 545−556.

[31] LAI T, XU J L, XIAO Q F, TONG Y X, HUANG J, ZHANG J P, LUO J M, LIU Y. Preparation and characterization of porous NiTi alloys synthesized by microwave sintering using Mg space holder[J]. Transactions of Nonferrous Metals Society of China, 2021, 31: 485−498.

[32] SCHALENBACH M, SPECK F D, LEDENDECKER M, KASIAN O, GOEHL D, MINGERS A M, BREITBACH B, SPRINGER H, CHEREVKO S, MAYRHOFER K J J. Nickel-molybdenum alloy catalysts for the hydrogen evolution reaction: Activity and stability revised [J]. Electrochimica Acta, 2018, 259(1): 1154−1161.

[33] LI G L, ZHANG X B, ZHANG H, LIAO C Y, JIANG G B. Bottom-up MOF-intermediated synthesis of 3D hierarchical flower-like cobalt-based homobimetallic phophide composed of ultrathin nanosheets for highly efficient oxygen evolution reaction [J]. Applied Catalysis B: Environmental, 2019, 249: 147−154.

[34] LI C L, ZHANG Z J, LIU R. In situ growth of 3D NiFe LDH-POM micro-flowers on nickel foam for overall water splitting [J]. Small, 2020, 16(46): 200377.

[35] WANG Q Y, ZHANG Y, NI W P, ZHANG Y, SUN T, ZHANG J H, DUAN J F, GAO Y, ZHANG S G. Free-standing phosphorous-doped molybdenum nitride in 3D carbon nanosheet towards hydrogen evolution at all pH values [J]. Journal of Energy Chemistry, 2020, 50: 44−51.

[36] HAN G H, KIM H, KIM J, KIM J, KIM S Y, AHN S H. Micro-nanoporous MoO_2@CoMo heterostructure catalyst for hydrogen evolution reaction [J]. Applied Catalysis B: Environmental, 2020, 270: 118895.

[37] MA X, WANG G W, QIN L F, LIU J, LI B, HU Y N, CHENG H F. Z-scheme g-C_3N_4-AQ-MoO_3 photocatalyst with unique electron transfer channel and large reduction area for enhanced sunlight photocatalytic hydrogen production [J]. Applied Catalysis B: Environmental, 2021, 288: 120025.

[38] DONG C L, YUAN X T, WANG X, LIU X Y, DONG W J, WANG R Q, DUAN Y H, HUANG F Q. Rational design of cobalt–chromium layered double hydroxide as a highly efficient electrocatalyst for water oxidation [J]. Journal of Materials Chemistry A, 2016, 4: 11292−11298.

[39] LIU G, WANG M H, WU Y, LI N, ZHAO F, ZHAO Q, LI J P. 3D porous network heterostructure NiCe@NiFe electrocatalyst for efficient oxygen evolution reaction at large current densities [J]. Applied Catalysis B: Environmental, 2020, 260: 118199.

[40] XU B, SUN Y Q, CHEN Z M, ZHAO S Y, YANG X D, ZHANG H J, LI C C. Facile and large-scale preparation of Co/Ni−MoO_2 composite as high-performance electrocatalyst for hydrogen evolution reaction [J]. International Journal of Hydrogen Energy, 2018, 43(45): 20721−20726.

[41] YANG L J, ZHAO X C, YANG R Z, ZHAO P X, LI Y T, YANG P, WANG J C, ASTRUC D. In-situ growth of carbon nanotubes on Ni/NiO nanofibers as efficient hydrogen evolution reaction catalysts in alkaline media [J]. Applied Surface Science, 2019, 491: 294−300.

[42] WANG J, GE X, SHAO L, ZHANG J, PENG D, ZOU G, HOU H, DENG W, XU S, JI X, ZHANG W. Reaction-driven

transformation of Ni/NiO hybrid structure into Ni single atoms [J]. Materials Today Energy, 2020, 17: 100436.
[43] LIU Z, ZENG L L, YU J Y, YANG L J, ZHANG J, ZHANG X L, HAN F, ZHAO L L, LI X, LIU H, ZHOU W J. Charge redistribution of Ru nanoclusters on Co_3O_4 porous nanowire via the oxygen regulation for enhanced hydrogen evolution reaction [J]. Nano Energy, 2021, 85: 105940.
[44] QIU Z, MA Y, EDVINSSON T. *In operando* Raman investigation of Fe doping influence on catalytic NiO intermediates for enhanced overall water splitting [J]. Nano Energy, 2019, 66: 104118.
[45] TOGHRAEI A, SHAHRABI T, DARBAND G B. Electrodeposition of self-supported Ni−Mo−P film on Ni foam as an affordable and high-performance electrocatalyst toward hydrogen evolution reaction [J]. Electrochimica Acta, 2020, 335: 135643.
[46] SUN Hui-ying, XU Guang-rui, LI Fu-min, HONG Qing-ling, JIN Pu-jun, CHEN Pei, CHEN Yu. Hydrogen generation from ammonia electrolysis on bifunctional platinum nanocubes electrocatalysts [J]. Journal of Energy Chemistry, 2020, 47: 234−240.
[47] ZHOU J, XIAO H S, WENG W, GU D, XIAO W. Interfacial confinement of Ni−V_2O_3 in molten salts for enhanced electrocatalytic hydrogen evolution [J]. Journal of Energy Chemistry, 2020, 50: 280−285.
[48] LIU Z, LI Z, LI J, XIONG J, ZHOU S F, LIANG J W, CAI W W, WANG C, YANG Z H, CHENG H S. Engineering of Ru/Ru_2P interfaces superior to Pt active sites for catalysis of the alkaline hydrogen evolution reaction [J]. Journal of Materials Chemistry A, 2019, 7: 5621−5625.
[49] SHANG Xiao, CHI Jing-qi, WANG Zhong-bing, DONG Bin, ZHAO Jin-chong, LI Xing-hua, YAN Kai-li, WANG Lei, CHAI Yong-ming, LIU Chen-guang. Microwave annealing promoted in-situ electrochemical activation of Ni_3S_2 nanowires for water electrolysis [J]. Journal of Catalysis, 2018, 368: 112−119.
[50] SHI Y M, ZHANG B. Recent advances in transition metal phosphide nanomaterials: Synthesis and applications in hydrogen evolution reaction [J]. Chemical Society Reviews, 2016, 45: 1529−1541.
[51] SHANG P F, YE Z G, DING Y, ZHU Z X, PENG X Y, MA G, LI D S. Nanosponge-like solid solution of NiMo with a high hydrogen evolution reaction performance over a wide range of current densities [J]. ACS Sustainable Chemistry and Engineering, 2020, 8(29): 10664−10672.
[52] WANG J, SHAO H T, REN S, HU A M, LI M. Fabrication of porous Ni−Co catalytic electrode with high performance in hydrogen evolution reaction [J]. Applied Surface Science, 2021, 539: 148045.
[53] DENG Z H, WANG J, NIE Y, WEI Z D. Tuning the interface of Ni@$Ni(OH)_2$/Pd/rGO catalyst to enhance hydrogen evolution activity and stability [J]. Journal of Power Sources, 2017, 352: 26−33.
[54] CHEN Z, CUMMINS D, REINECKE B N, CLARK E, SUNKARA M K, JARAMILLO T F. Core-shell MoO_3−MoS_2 nanowires for hydrogen evolution: A functional design for electrocatalytic materials [J]. Nano Letters, 2011, 11(10): 4168−4175.

多孔块体 NiMo 合金原位水热合成 Ni−MoO_2 异质结构以实现高效析氢反应

唐 剑[1]，徐吉林[1]，李亮亮[1]，马永存[1]，叶志国[1]，罗弘宇[2]，罗军明[1]

1. 南昌航空大学 材料科学与工程学院，南昌 330063；
2. 澳门科技大学 商学院，澳门 999078

摘 要：通过简便的粉末冶金和水热法在多孔块体 NiMo 合金上原位合成 Ni−MoO_2 异质结构电催化剂。场发射扫描电镜、透射电镜及 X 射线光电子能谱分析结果表明：经过水热处理后，制备的 Ni−MoO_2 电极具有异质结构并且在其表面同时形成一层 $Ni(OH)_2$ 纳米片，这种异质结构和纳米片层提供丰富的界面、更多的活性中心和更大的活性比表面积。析氢反应结果表明，Ni−MoO_2 异质结构表现出优异的催化性能，仅需 41 mV 的过电位即可达到 10 mA/cm^2 的电流密度，并且具有 52.7 mV/dec 的低 Tafel 斜率和在碱性介质中具有优异的稳定性。

关键词：析氢反应；Ni−MoO_2 异质结构；粉末冶金；多孔块体电催化剂；NiMo 合金

(Edited by Bing YANG)